Giant Photocurrent Enhancement by Coulomb Interaction in a Single Quantum Dot for Energy Harvesting

Kai Peng,[1,2] Shiyao Wu,[1,2] Xin Xie,[1,2] Jingnan Yang,[1,2] Chenjiang Qian,[1,2] Feilong Song,[1,2] Sibai Sun,[1,2] Jianchen Dang,[1,2] Yang Yu,[1,2] Shushu Shi,[1,2] Jiongji He,[1,2] and Xiulai Xu[1,2,3,*]

[1]*Beijing National Laboratory for Condensed Matter Physics, Institute of Physics, Chinese Academy of Sciences, 100190 Beijing, China*

[2]*CAS Center for Excellence in Topological Quantum Computation and School of Physical Sciences, University of Chinese Academy of Sciences, 100049 Beijing, China*

[3]*Songshan Lake Materials Laboratory, Dongguan, 523808 Guangdong, China*

Understanding the carrier excitation and transport processes at the single-charge level plays a key role in quantum-dot-based solar cells and photodetectors. Here we report on Coulomb-induced giant photocurrent enhancement of positively charged trions (X^+) in a single self-assembled InAs/GaAs quantum dot embedded in an *n-i* Schottky device by high-resolution photocurrent spectroscopy. The Coulomb repulsion between the two holes in X^+ increases the tunneling rate of one hole, and the remaining hole can be reused as the initial state to regenerate X^+. This process results in the photocurrent amplitude of X^+ being up to 30 times larger than that of the neutral exciton. The analysis of the hole tunneling time gives the equivalent change of hole tunnel barriers caused by Coulomb interaction between two holes as 8.05 meV during the tunneling process. Our work provides a fundamental understanding of energy conversion for solar cells on the nanoscale to increase internal quantum efficiency for energy harvesting.

I. INTRODUCTION

Semiconductor quantum dots (QDs) have attracted much attention as third-generation photovoltaic solar cells due to the potential ultrahigh energy-conversion efficiency [1,2]. Various approaches have been investigated intensively to increase the efficiency, such as intermediate-band excitation using low-energy photons [3–6], enhancing electron transfer in sensitized solar cells [7–12], or producing multiple excitons per single photon [13–16]. The dissociation of photogenerated excitons into free electrons and holes plays a key role in solar cells and photodetectors [17], which is affected by the strong Coulomb interactions between the carriers in the nanoscale systems. Much research has focused on the mechanism of dissociation against the Coulomb attraction between electrons and holes in low-dimensional nanostructures [15,18–23]. During exciton excitation and dissociation, various excitons consisting of different numbers of electrons and holes can be generated. The effect of Coulomb repulsion between these carriers in solar cells has rarely been explored. Recently, a strong enhancement of conversion efficiency with built-in electrons of an intermediate-band QD solar cell was reported [24]. Generally, the Coulomb repulsion

between the electrons (holes) in the conduction (valance) band can accelerate the tunneling rate of electrons (holes), but the mechanism still needs to be investigated quantitatively. Photocurrent (PC) spectroscopy of a single QD at low temperature is a powerful method to investigate the hole-spin-based qubit in quantum-information processing [25–27] or the photon absorption and carrier tunneling process in QD-based solar cells [28], which offers a profound understanding of the carrier dynamics in the applications of solar cells and photodetectors based on QDs at the single-charge level.

In this paper, we demonstrate Coulomb-induced giant PC enhancement in a single InAs/GaAs QD by high-resolution PC spectroscopy of positively charged trions (X^+). The QDs are embedded in the intrinsic region of an *n-i* Schottky photodiode based on a two-dimensional electron gas (2DEG). Two-color continuous-wave narrow-bandwidth (approximately 1 MHz) lasers are used to obtain the high-resolution PC spectra of X^+, which are measured by our sweeping the neutral exciton (X^0) and X^+ transition energies simultaneously through the quantum-confined Stark effect (QCSE) to achieve resonant excitation. The Coulomb repulsion between the two holes in X^+ increases the tunneling rate of one hole, and the remaining hole can be reused as the initial state to excite X^+ again. This process enhances the PC amplitude of X^+

*xlxu@iphy.ac.cn

024015-1

such that it is dozens of times larger than that of X^0. The saturation behavior in the pumping-power-dependent PC measurements is intuitively interpreted by a four-level-rate-equation model, from which the hole tunneling time for X^+ and X^0 is obtained precisely. By repeating the measurements for a range of excitation energies, we obtain the hole tunneling time as a function of the vertical electric field. The Wentzel-Kramers-Brillouin (WKB) approximation is used to determine the hole tunnel barriers in the *s* shell of the valence band for single- and double-hole cases quantitatively, which shows a change of 8.05 meV of the tunnel barrier caused by hole repulsion. These results can be used to increase the photoelectric conversion efficiency and photoresponse in the applications of solar cells and photodetectors based on QDs.

II. EXPERIMENTAL DETAILS

The *n-i* Schottky device is designed and fabricated for PC measurement of single QDs; the device structure is shown schematically in Fig. 1(a). A single layer of InAs self-assembled QDs is grown by molecular beam epitaxy, and is embedded in a 250-nm-thick GaAs layer with a low density of about 10^9 cm^{-2}. A Si-δ-doped GaAs layer is located 50 nm below with a doping density $N_d = 5 \times 10^{12}$ cm^{-2}, forming a 2DEG. The Schottky contact is formed by our evaporating a 10-nm semitransparent Ti at the surface, followed by a Al mask with apertures of about 1–3 μm. A (Au,Ge)Ni Ohmic contact is fabricated to connect the 2DEG with the Cr/Au bond pads. Moreover, a distributed Bragg reflector with 13 pairs of Al$_{0.94}$Ga$_{0.06}$As/GaAs (67/71 nm) is grown at the bottom of the structure to enhance the photon collection efficiency. The vertical electric field can be applied on the QDs as $F = (V_i - V_b)/d$, where V_i, V_b, and d are the built-in potential (0.74 V for this device), the applied bias voltage, and the distance between the Schottky contact and the 2DEG, respectively.

The device is placed on an *xyz* piezoelectric stage in a helium-gas-exchange cryostat at 4.2 K. A confocal microscope with a microscope objective with a large numerical aperture of 0.82 is used to perform microphotoluminescence and PC measurements for single QDs. Nonresonant excitation is achieved by use of a 650-nm semiconductor laser for photoluminescence (PL) measurement, and two tunable narrow-bandwidth (approximately 1 MHz) external-cavity diode lasers in the Littrow configuration are used to achieve resonant excitation. The PL signals of QDs are collected and dispersed through a 0.55-m spectrometer, and are detected by a liquid-nitrogen-cooled charge-coupled-device camera with a spectral resolution of about 60 μeV. A semiconductor analyzer with high current resolution (10 fA) is used to measure the current.
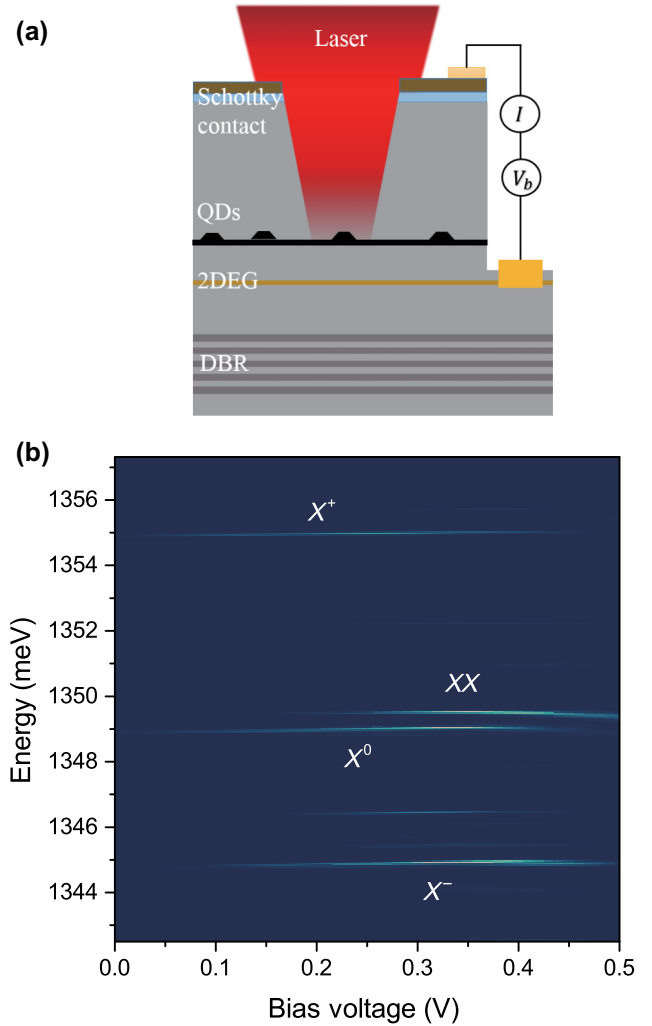

FIG. 1. The device structure and bias-dependent microphotoluminescence spectra of a single QD. (a) The *n-i* Schottky photodiode based on a 2DEG. (b) Bias-dependent microphotoluminescence spectra of the single QD, showing PL from X^+, XX, X^0, and X^-. DBR, distributed Bragg reflector.

III. RESULTS AND DISCUSSION

Before the PC measurements are conducted, bias-dependent microphotoluminescence spectroscopy is performed on a single QD with above-band excitation to identify the transition energies of different charged exciton states and the bias voltage range for the PC regime, as shown in Fig. 1(b). The X^0 and the biexciton (XX) peaks have fine-structure splitting caused by the electron-hole exchange interaction and structure asymmetry of the QD [29], and the X^0 PL intensity reaches saturation earlier than that of XX. These behaviors help us to identify the X^0 and XX peaks. The charged trions can be identified by the binding energies and the electric-field-dependent behaviors. At the high positive bias voltages in Fig. 1(b), which correspond to low electric fields, the *s*-shell electron

state is below the Fermi level in the 2DEG. The QDs will be charged with one electron that tunneled from the 2DEG [30]. As a result, the negatively charged trion X^- dominates. With increase of the electric field, the s-shell electron level is above the Fermi level, and the electron charging stops. Instead, the tilt of the energy band makes the tunneling rate of captured electrons in the QDs faster than that of holes, resulting in the accumulation of holes in the QDs and the observation of positively charged trions X^+. When the electric field is strong enough to let the hole tunnel out of the QD before recombination with an electron, the PL peaks of the QD disappear. In this regime, the PC can be observed.

In the experiment, the PC spectra are measured by our sweeping the exciton transition energy by the QCSE to resonate with the fixed laser energy. The Stark effect can be described as $E(F) = E(0) + pF + \beta F^2$, where $E(0)$ is the transition energy without the external applied field, p is the permanent dipole moment, and β is the polarizability of electron-hole wavefunctions. This is a convenient way to tune the transition energies of X^0 and X^+ simultaneously. For X^0, the energy-band structures during the excitation and tunneling processes are shown in the top panel in Fig. 2(b). The QD s shell is empty without laser shining at negative bias voltages. The continuous-wave laser with energy E_L^0 can excite the QD from the ground state $|g\rangle$ to $|X^0\rangle$ resonantly. Then the electron in the conduction band and the hole in the valence band will tunnel out of the QD under the electric field, contributing to a measurable PC signal. As a result, the system is empty again and ready
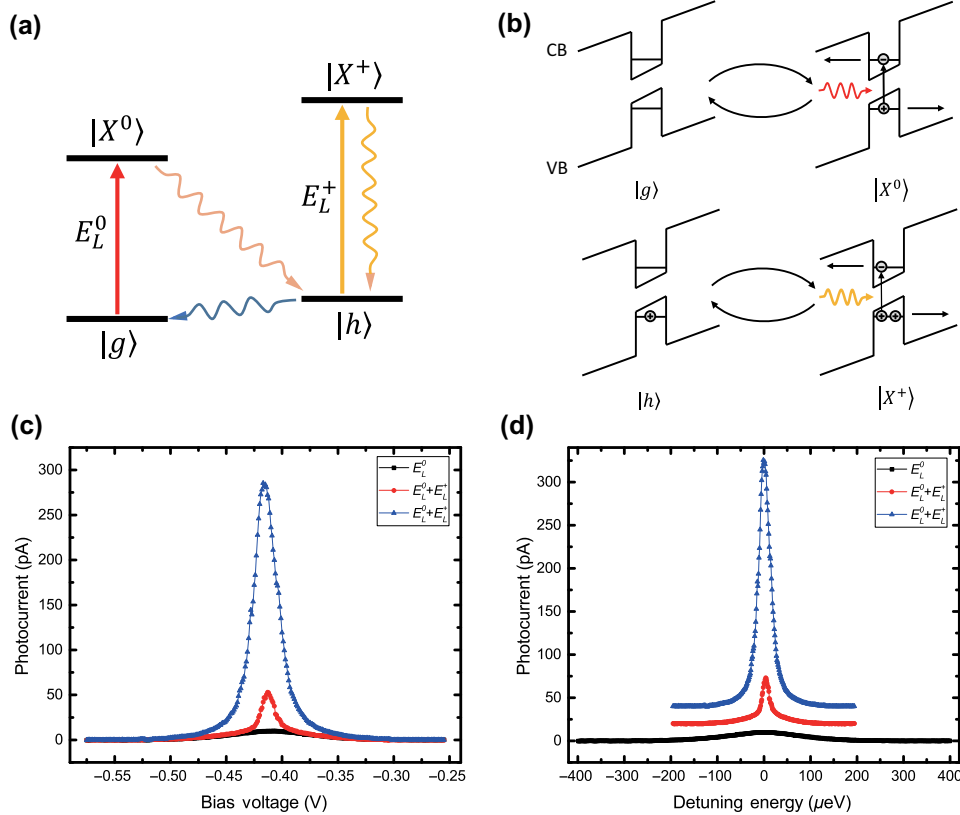

FIG. 2. The PC measurements and the PC spectra of X^0 and X^+ from a single QD. (a) Two-color-excitation scheme used for X^+ PC measurements. The straight arrows represent the excitation and the wavy arrows represent the tunneling processes of carriers. $|g\rangle$ represents the ground state of the QD, which can be excited to the neutral exciton state $|X^0\rangle$ resonantly through the first continuous-wave laser with energy E_L^0. The electron of X^0 tunnels out of the QD and a hole is left as $|h\rangle$. The second continuous-wave laser (E_L^+) is used to excite the system to $|X^+\rangle$. Then the electron and one hole in X^+ tunnel out of the dot and the system decays to the single-hole state $|h\rangle$. The excitation from $|h\rangle$ to $|X^+\rangle$ can happen again. The single hole may tunnel out of the QD, and this brings the system back to $|g\rangle$ for the next two-color-excitation cycle. The two lasers are both linearly polarized, which ensures that all the spin states can be excited for both X^0 and X^+. (b) PC for X^0 (top) and X^+ (bottom). (c) PC spectra under two-color excitation. The black squares represent the net X^0 PC spectrum with $E_L^0 = 1347.68$ meV; the red circles and the blue triangles represent the measured PC spectra under two-color excitation with $E_L^+ = 1354.05$ meV at low and high excitation powers (50 and 1500 arbitrary units, respectively), respectively. (d) The PC spectra from (c) replotted as a function of detuning energy. The bias voltage (electric field) is replaced with energy through different QCSEs for X^0 and X^+. The effect of Coulomb attraction of the extra hole on the electron-induced linewidth narrowing is clearer. The spectra are shifted for clarity.

for the next excitation [31]. For X^+, the exciton energy is renormalized due to the Coulomb interactions caused by the extra hole. In addition, X^+ requires a single hole as the initial state, and the two-color-resonant-excitation scheme is needed, as shown in Fig. 2(a). Firstly, X^0 is excited by a laser labeled as E_L^0 resonantly. Because of fast tunneling rate of electrons in the presence of an electric field, the system will decay to the single-hole state $|h\rangle$ in several picoseconds as the initial state of X^+. Meanwhile, the second laser with higher energy (E_L^+) pumps the QD to the $|X^+\rangle$ state. This is the two-color-excitation scheme for X^+.

There are different possible paths for the decay of X^+. As mentioned above, the electron will tunnel out fast preferentially. For the tunneling of holes, one hole tunnels out quickly due to the Coulomb repulsion between the two holes, and the system decays to $|h\rangle$. The remaining hole decays to the ground state $|g\rangle$ very slowly, which makes the $|h\rangle$ state a metastable state to be excited to $|X^+\rangle$ again when the angular momentum condition is fulfilled, as the bottom panel in Fig. 2(b) shows. Therefore, this $|X^+\rangle \rightarrow |h\rangle \rightarrow |X^+\rangle$ self-circulation process ensures that the excitation of X^+ does not totally depend on the $|X^0\rangle \rightarrow |h\rangle$ decay process. However, it is still possible that the single hole tunnels out and the system returns to $|g\rangle$. In this case, the next two-color-excitation loop can happen again. The net X^+ PC signal is from the $|X^+\rangle \rightarrow |h\rangle$ decay process, as shown in the bottom panel in Fig. 2(b). Actually these two competitive decay paths coexist, which is why the two-color excitation is still needed although the circulation has already started. It is worth noting that the spins of the carrier are ignored in the two-color-excitation scheme. Here linearly polarized narrow-linewidth lasers are chosen to pump X^0 and X^+ resonantly; thus, all the spin states can be excited for both X^0 and X^+ compared with the cross-circular-polarized scheme for spin-resolved excitation in previous work [27,32].

Figure 2(c) shows the measured PC signals with the two-color excitation. The energy of the first laser for exciting X^0 is fixed at $E_L^0 = 1347.68$ meV. The black points represent the X^0 PC spectrum with only one laser exciting X^0. When the second laser, with energy (E_L^+) of 1354.05 meV, is applied, the X^+ PC components are added to the PC peak signal as the red and blue curves shown in Fig. 2(c) for low and high pumping power (50 and 1500 arbitrary units, respectively), respectively. The fitted Lorentzian curve of the PC spectrum gives the corresponding central voltage on resonance, as well as the linewidth and the amplitude. The most-striking feature of the two-color-excitation PC signals is the giant enhancement of the PC amplitude, which is also observed for other QDs in similar Schottky devices in our experiments. Here the PC amplitude of X^+ is surprisingly more than 1 order of magnitude larger than that of X^0 at high excitation power, while previous work with a cross-circular-polarized

scheme for spin-selection excitation could achieve a PC amplitude of X^+ only comparable with that of X^0 [27,32]. One reason is that the reuse of the hole from X^+ under linearly polarized excitation can partly remove the limit of the hole decay from X^0. For the circularly-polarized-excitation scheme, the reuse of the hole may not happen if this hole's transition needs perpendicular circularly polarized excitation. More importantly, the Coulomb repulsion between the two holes increases the tunneling rate and greatly enhances the PC amplitude. Part of the PC signal shown as the blue points in Fig. 2(c) is from X^0, but this component can be ignored. Because at high excitation power, the $|X^+\rangle \rightarrow |h\rangle \rightarrow |X^+\rangle$ self-circulation as shown in the bottom panel in Fig. 2(b) dominates, the excitation of X^0 is restricted and its PC component is smaller than the net X^0 PC amplitude, which is already more than 1 order of magnitude smaller than that of X^+.

To verify the Coulomb interactions between the extra hole in X^+ and other carriers, the linewidth of the PC spectrum is analyzed. The extra hole in X^+ increases the Coulomb attraction to the electron, which prolongs the tunneling time of the electron and decreases the linewidth of the X^+ PC spectrum, as shown clearly in Fig. 2(d), in which the x axis is replaced with the detuning energy through the different Stark effects of X^0 and X^+. Both lasers are tuned simultaneously to obtain a series of PC spectra with different electric fields, and the correlations of the transition energies and electric fields for X^0 and X^+ are built through a quadratic fit according to the QCSE. Here the linewidth of the X^+ PC spectrum at low pumping power (red points) is about 20 μeV. If we ignore the power broadening at low pumping power and assume that electron tunneling is the main dephasing mechanism, the linewidth corresponds to a tunneling time of the electron in X^+ of about 30 ps. In contrast, the linewidth of the X^0 PC spectrum is about 190 μeV in Fig. 2(d). If we deduct the power broadening, the tunneling time of the electron in X^0 is about several picoseconds, corresponding to the fast tunneling process from $|X^0\rangle$ to $|h\rangle$ shown in Fig. 2(a).

To demonstrate the giant enhancement of the PC amplitude under two-color excitation and the Coulomb interaction between two holes in X^+ quantitatively, power-dependent PC measurements are performed. The saturation behavior in the power-dependent measurement is a simple way to investigate the characteristic time of the system, and has been widely used in QD research [33–38]. Here the long tunneling time of the hole limits the PC amplitudes for both X^0 and X^+. For the X^0 PC measurement, before the hole tunnels out of the QD, the next electron-hole pair cannot be excited resonantly by the same laser because of the energy detuning between different excitons. Therefore, saturation of the PC amplitude of X^0 can be observed with the increase of the pumping power at a fixed electric field, as shown in Fig. 3(b) (red line with circles). The saturation effect of the PC amplitude can be described
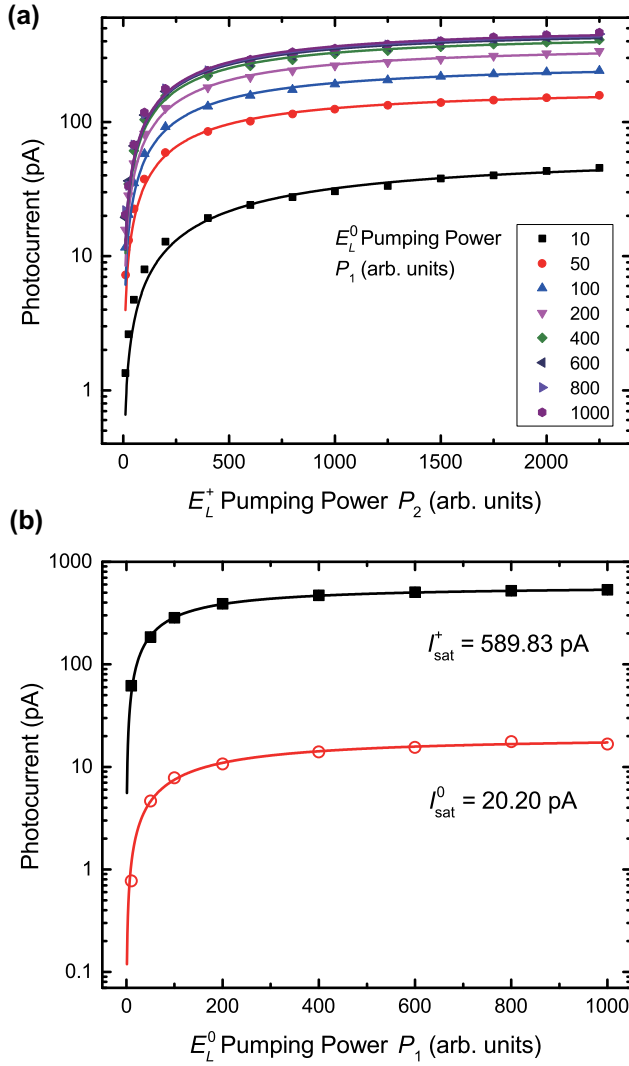
FIG. 3. Pumping-power-dependent PC amplitudes of X^0 and X^+. (a) The E_L^+-pumping-power-dependent PC amplitude of X^+ for a series of E_L^0 pumping powers P_1. (b) The E_L^0-pumping-power-dependent PC amplitudes of X^+ and X^0, corresponding to the squares and circles, respectively. The curves are the fitted results obtained with Eq. (1).

by the following theoretical model [39]:

$$I_{\text{peak}} = \frac{e}{2\tau_{\text{esc}}^h} \frac{\widetilde{P}}{\widetilde{P} + P_0} = I_{\text{sat}}^0 \frac{\widetilde{P}}{\widetilde{P} + P_0}, \qquad (1)$$

where $\widetilde{P}$ is the laser pumping power on the QD (arbitrary units), P_0 is the renormalized coefficient, e is the elementary charge, and τ_{esc}^h is the hole tunneling time. The power-dependent X^0 PC amplitudes can be fitted by this model very well, as the red curve in Fig. 3(b). At $F = 46$ kV/cm, the saturation PC amplitude I_{sat}^0 is 20.20 pA, which corresponds to a hole tunneling time of 3.96 ns.

For X^+, it is more complicated. The two-color-excitation scheme makes the PC amplitude of X^+ depend

not only on the pumping power of the laser resonant with X^+ but also on the laser used to excite X^0. Furthermore, the measured PC signals include the components from X^+ and X^0, and the fast electron-tunneling process from $|X^0\rangle$ to $|h\rangle$ also affects the preparation of X^+. To describe the dynamics in the two-color-excitation scheme shown in Fig. 2(a) precisely, we build the following four rate equations:

$$\frac{dN_+}{dt} = -\frac{N_+}{\tau_{\text{esc}}^+} - B_{+h}N_+\rho_2 + B_{h+}N_h\rho_2, \qquad (2a)$$

$$\frac{dN_h}{dt} = \frac{N_+}{\tau_{\text{esc}}^+} + B_{+h}N_+\rho_2 - B_{h+}N_h\rho_2 - \frac{N_h}{\tau_{\text{esc}}^h} + \frac{N_x}{\tau_{\text{esc}}^x}, \qquad (2b)$$

$$\frac{dN_x}{dt} = -B_{xg}N_x\rho_1 - \frac{N_x}{\tau_{\text{esc}}^x} + B_{gx}N_g\rho_1, \qquad (2c)$$

$$\frac{dN_g}{dt} = \frac{N_h}{\tau_{\text{esc}}^h} + B_{xg}N_x\rho_1 - B_{gx}N_g\rho_1. \qquad (2d)$$

Here N_+, N_h, N_x, and N_g are the time-averaged occupation numbers of $|X^+\rangle$, $|h\rangle$, $|X^0\rangle$, and $|g\rangle$, respectively. B_{+h}, B_{h+}, B_{xg}, and B_{gx} are the stimulated-emission and absorption coefficients, so we can set $B_{+h} = B_{h+} = B_2$ and $B_{xg} = B_{gx} = B_1$. ρ_1 and ρ_2 are the energy densities of the radiation field corresponding to the transitions of X^0 and X^+, respectively, and they can be expressed in terms of the pumping power P_1 and P_2. The decay processes are introduced by τ_{esc}^+, τ_{esc}^h, and τ_{esc}^x, where τ_{esc}^+ and τ_{esc}^h correspond to the hole tunneling time for double- and single-hole cases, respectively. The fast tunneling process from $|X^0\rangle$ to $|h\rangle$ is described by τ_{esc}^x, which is the tunneling time of the electron in X^0. In this model, spontaneous emission is ignored in the electric field regime for PC measurement. The steady-state solutions can be obtained by our considering the relation $N_+ + N_h + N_x + N_g = 1$. The PC amplitude in the experiment can be described as

$$I = e\left(\frac{N_h}{\tau_{\text{esc}}^h} + \frac{N_+}{\tau_{\text{esc}}^+}\right), \qquad (3)$$

where N_h/τ_{esc}^h and N_+/τ_{esc}^+ correspond to the tunneling processes of X^0 and X^+, respectively, shown in Fig. 2(b).

Under the two-color-excitation scheme, the PC amplitude depends on the pumping power of the laser resonant with X^+ (P_2) and the laser used to excite X^0 (P_1). To get the hole tunneling time of X^+, we perform two-step power-dependent measurements. At the beginning, we increase P_2 with fixed P_1, so the saturation PC amplitude can be obtained through the saturation behavior, which has the same form as Eq. (1). Then a series of measurements for different values of P_1 are performed, as shown in Fig. 3(a), which gives the saturation PC amplitudes with the increase of P_1, as shown by the black line with squares in Fig. 3(b). Through the rate-equation model, the

two-step power-dependent scheme gives the saturation PC amplitude in two-color excitation as

$$I_{sat}^+ = \frac{e}{2\tau_{esc}^+}\frac{\tau_{esc}^h + \tau_{esc}^+}{\tau_{esc}^h + \tau_{esc}^x} \approx \frac{e}{2}\left(\frac{1}{\tau_{esc}^+} + \frac{1}{\tau_{esc}^h}\right). \quad (4)$$

Here the fast electron-tunneling time τ_{esc}^x of about several picoseconds is ignored in Eq. (4) compared with the hole tunneling time τ_{esc}^h of several nanoseconds. The saturation behaviors can be described very well with the model in Eq. (4). Here the saturation PC amplitude under two-color excitation is fitted as $I_{sat}^+ = 589.83$ pA, corresponding to a hole tunneling time for the double-hole case τ_{esc}^+ of 0.14 ns, almost 30 times faster than that for the single-hole case, $\tau_{esc}^h = 3.96$ ns.

It is not surprising that the saturation PC amplitude under two-color excitation depends on the tunneling rates of holes for the single- and double-hole cases shown in Eq. (4). The difference of up to 30 times in the tunneling rates proves that there is enough time for $|h\rangle$ to be excited to $|X^+\rangle$ mostly rather than decay to $|g\rangle$, as shown in Fig. 2(a). The hole tunneling time in X^+ (0.14 ns) is still much longer than the electron tunneling time (approximately 30 ps), so the first hole tunneling process restricts the PC amplitude of X^+. Here at saturation, the $|X^+\rangle \rightarrow |h\rangle \rightarrow |X^+\rangle$ self-circulation process dominates the X^+ excitation and tunneling processes, and the hole tunneling time when the two holes occupy the valance-band ground state limits the PC amplitude of X^+.

Obviously, the hole tunneling time τ_T^h is dependent on the electric field applied across the QD. We now repeat the power-dependent PC measurements of X^0 and X^+ for a series of electric fields by tuning the pumping laser energies E_L^0 and E_L^+, which gives the saturation PC amplitude and the hole tunneling time as a function of the electric field for the single- and double-hole cases, as shown in Fig. 4. τ_T^h can be tuned by more than 1 order of magnitude in the measured range of electric fields. For the QD, the hole tunneling rate R_T^h (τ_T^{h-1}) can be described by a one-dimensional (1D) (along the growth direction) WKB approximation [28,40,41]:

$$R_T^h = \frac{\hbar\pi}{2m_h^* H^2} \exp\left(\frac{-4}{3\hbar eF}\sqrt{2m_h^* E_b^3}\right), \quad (5)$$

where $m_h^* = 0.59 m_e$ is the heavy-hole effective mass in GaAs along the growth direction and m_e is the electron mass in a vacuum, H is the QD height, F is the vertical electric field, and E_b is the tunnel barrier height or the ionization energy for the hole. Even though the QDs have three-dimensional confinements, the confinement along the growth direction is much stronger than the confinement in the QD plane. From the high-resolution cross-section image of a single QD from the same sample obtained by transmission electron microscopy shown in Ref. [42], the
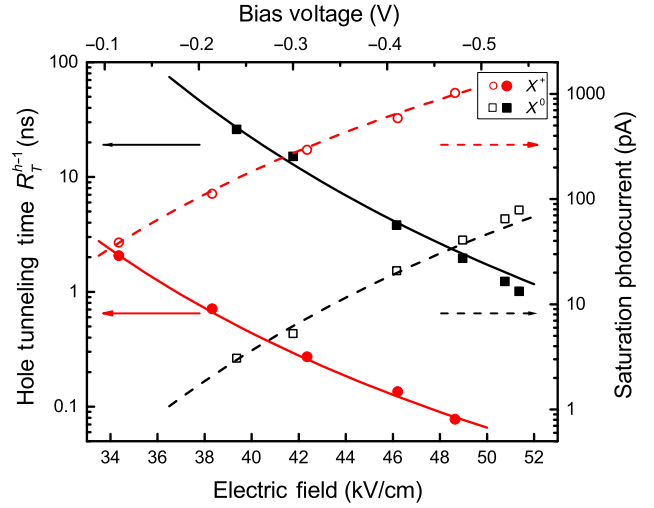

FIG. 4. Hole tunneling time $R_T^{h^{-1}}$ and saturation PC I_{peak} as a function of the electric field (bias voltage). The solid and dashed lines are the fittings obtained with the theoretical model in Eq. (5) based on the 1D WKB approximation, yielding $E_b^0 = 45.51$ meV and $E_b^+ = 37.46$ meV with a QD height of 4.5 nm.

height of the QD is 5 nm and its base length is about 20 nm. On the other hand, the electric field is applied along the growth direction, so the 1D model is reasonable to describe the tunneling behavior in QDs along the growth direction. This model in Eq. (5) agrees very well with the experimental data for electron and hole tunneling rates in previous work [33,34]. As a device with the same structure, the QD height of 4.5 nm is chosen here to fit the experimental data shown in Fig. 4. The hole tunneling time and saturation PC of X^0, as shown by black points in Fig. 4, give the fitted tunnel barrier E_b^0 of the single hole as 45.51 meV, which is consistent with previous work [34]. Since X^+ has two holes, the decay to the single-hole state has two tunneling channels, which results in the tunneling rate being twice as fast as for single-hole tunneling without consideration of Coulomb interaction between the two holes. So the hole tunneling rate for the two-hole case should be halved in Eq. (5) to fit the tunnel barrier E_b^+. Here the value of E_b^+ is 37.46 meV when two holes coexist. So equivalently, the Coulomb repulsion between the two holes results in a change of about 8.05 meV in the tunnel barrier, which describes the hole Coulomb repulsion interaction in the tunneling process quantitatively. It is similar to the binding energy in PL of about 6 meV as shown in Fig. 1(b).

As shown in Fig. 4, the hole tunneling rate of X^+ is more than 1 order of magnitude larger than that of X^0 in a large range of electric fields. In a low electric field, the Coulomb interaction is more significant. With the 1D WKB model in Eq. (5) with the fitted parameters, the extrapolated hole tunneling rate for two holes is more than 2 orders of magnitude larger than that for a single hole at zero bias voltage. For the QDs studied, we can prepare

X^+ and investigate the hole-hole Coulomb interaction due to the dominant tunneling of holes in the dissociation of excitons in a single QD through PC spectroscopy. We believe that this mechanism also works for the electron case with a redesigned device structure. Although this QD device is not designed for solar cells particularly, the results strongly suggest that the Coulomb-induced giant enhancement of the PC signal can work for the application of QD-based solar cells (with zero bias voltage), especially for the right QD size for Coulomb energy and suitable barrier height. For practical applications for QD-based solar cells, p- or n-doped QDs can be obtained by the growing of a two-dimensional-hole-gas or 2DEG layer close to the QD layer to prepare positively or negatively charged trions, respectively. For example, a 50% increase of conversion efficiency in intermediate-band QD solar cells with n doping has been reported [24], where the interelectron Coulomb interaction can transfer electrons to the conducting state. Furthermore, we believe that this mechanism of Coulomb-induced enhancement of tunneling can be extended to colloidal-QD-based and perovskite-nanocrystal-based solar cells even though the strength of Coulomb interactions between carriers might be different.

IV. CONCLUSION

In conclusion, we demonstrate the Coulomb-induced giant enhancement of X^+ PC in a single InAs/GaAs QD under the two-color-excitation scheme. High-resolution PC spectra of X^+ are obtained by our sweeping the X^0 and X^+ transition energies to match the fixed narrow-bandwidth lasers by the QCSE simultaneously. The Coulomb repulsion between the two holes in X^+ greatly enhances the tunneling rate of one hole, and the remaining hole can be reused to build the $|X^+\rangle \rightarrow |h\rangle \rightarrow |X^+\rangle$ self-circulation process under the linearly-polarized-excitation scheme. This process increases the PC amplitude of X^+ by up to 30 times with respect to that of X^0. The hole tunneling times of X^+ and X^0 are successfully extracted from the saturation PC amplitude in the pumping-power-dependent PC spectra according to a four-level-rate-equation model. The hole tunneling time as a function of the electric field is obtained by our performing measurements for a range of bias voltages. By using the 1D WKB approximation model with a reasonable QD height, we fit the tunnel barrier heights for single- and double-hole cases. The results show that the Coulomb repulsion results in a change of about 8.05 meV in the tunnel barrier, which greatly enhances the hole tunneling rate. This quantitative investigation of the Coulomb interactions in few-particle states and the giant enhancement of the PC amplitude in a single QD with only a single extra charge could have great application for hole-spin-based quantum-information processing, and also provide a method to enhance the conversion efficiency for energy harvesting in solar cells and photodetectors based on semiconductor QDs.

[1] M. A. Green, *Third Generation Photovoltaics* (Springer, Berlin, 2006).

[2] A. Martí and A. Luque, *Next Generation Photovoltaics: High Efficiency through Full Spectrum Utilization* (Institute of Physics, Bristol, 2003).

[3] A. Luque and A. Martí, Increasing the Efficiency of Ideal Solar Cells by Photon Induced Transitions at Intermediate Levels, Phys. Rev. Lett. **78,** 5014 (1997).

[4] S. Tomić, Intermediate-band solar cells: Influence of band formation on dynamical processes in InAs/GaAs quantum dot arrays, Phys. Rev. B **82,** 195321 (2010).

[5] A. Luque, A. Martí, and C. Stanley, Understanding intermediate-band solar cells, Nat. Photonics **6,** 146 (2012).

[6] Y. Okada, N. J. Ekins-Daukes, T. Kita, R. Tamaki, M. Yoshida, A. Pusch, O. Hess, C. C. Phillips, D. J. Farrell, K. Yoshida, N. Ahsan, T. Shoji, T. Sogabe, and J.-F. Guillemoles, Intermediate band solar cells: Recent progress and future directions, Appl. Phys. Rev. **2,** 021302 (2015).

[7] L. J. Diguna, Q. Shen, J. Kobayashi, and T. Toyoda, High efficiency of CdSe quantum-dot-sensitized TiO$_2$ inverse opal solar cells, Appl. Phys. Lett. **91,** 023116 (2007).

[8] P. V. Kamat, Quantum dot solar cells. semiconductor nanocrystals as light harvesters, J. Phys. Chem. C **112,** 18737 (2008).

[9] A. Kojima, K. Teshima, Y. Shirai, and T. Miyasaka, Organometal halide perovskites as visible-light sensitizers for photovoltaic cells, J. Am. Chem. Soc. **131,** 6050 (2009).

[10] V. González-Pedro, X. Xu, I. Mora-Seró, and J. Bisquert, Modeling high-efficiency quantum dot sensitized solar cells, ACS Nano **4,** 5783 (2010).

[11] P. V. Kamat, Quantum dot solar cells. The next big thing in photovoltaics, J. Phys. Chem. C **4,** 908 (2013).

[12] Z. Pan, I. Mora-Ser oó, Q. Shen, H. Zhang, Y. Li, K. Zhao, J. Wang, X. Zhong, and J. Bisquert, High-efficiency 'green' quantum dot solar cells, J. Am. Chem. Soc **136,** 9203 (2014).

[13] A. Nozik, Quantum dot solar cells, Physica E **14,** 115 (2002).

[14] R. D. Schaller and V. I. Klimov, High Efficiency Carrier Multiplication in PbSe Nanocrystals: Implications for Solar Energy Conversion, Phys. Rev. Lett. **92,** 186601 (2004).

[15] R. J. Ellingson, M. C. Beard, J. C. Johnson, P. Yu, O. I. Micic, A. J. Nozik, A. Shabaev, and A. L. Efros, Highly

efficient multiple exciton generation in colloidal PbSe and PbS quantum dots, Nano Lett. **5,** 865 (2005).

[16] R. D. Schaller, M. Sykora, J. M. Pietryga, and V. I. Klimov, Seven excitons at a cost of one: Redefining the limits for conversion efficiency of photons into charge carriers, Nano Lett. **6,** 424 (2006).

[17] G. D. Scholes and G. Rumbles, Excitons in nanoscale systems, Nat. Mater. **5,** 683 (2006).

[18] M. Muntwiler, Q. Yang, W. A. Tisdale, and X.-Y. Zhu, Coulomb Barrier for Charge Separation at an Organic Semiconductor Interface, Phys. Rev. Lett. **101,** 196403 (2008).

[19] J. Pijpers, R. Ulbricht, K. Tielrooij, A. Osherov, Y. Golan, C. Delerue, G. Allan, and M. Bonn, Assessment of carrier-multiplication efficiency in bulk PbSe and PbS, Nat. Phys. **5,** 811 (2009).

[20] S. Gélinas, A. Rao, A. Kumar, S. L. Smith, A. W. Chin, J. Clark, T. S. van der Poll, G. C. Bazan, and R. H. Friend, Ultrafast long-Range charge separation in organic semiconductor photovoltaic diodes, Science, **343,** 512 (2014).

[21] A. E. Jailaubekov, A. P. Willard, J. R. Tritsch, W.-L. Chan, N. Sai, R. Gearba, L. G. Kaake, K. J. Williams, K. Leung, P. J. Rossky, and X.-Y. Zhu, Hot charge-transfer excitons set the time limit for charge separation at donor/acceptor interfaces in organic photovoltaics, Nat. Mater. **12,** 66 (2013).

[22] A. C. Jakowetz, M. L. Böhm, A. Sadhanala, S. Huettner, A. Rao, and R. H. Friend, Visualizing excitations at buried heterojunctions in organic semiconductor blends, Nat. Mater. **16,** 551 (2017).

[23] J.-C. Blancon, H. Tsai, W. Nie, C. C. Stoumpos, L. Pedesseau, C. Katan, M. Kepenekian, C. M. M. Soe, K. Appavoo, M. Y. Sfeir, S. Tretiak, P. M. Ajayan, M. G. Kanatzidis, J. Even, J. J. Crochet, and A. D. Mohite, Extremely efficient internal exciton dissociation through edge states in layered 2D perovskites, Science **355,** 1288 (2017).

[24] K. A. Sablon, J. W. Little, V. Mitin, A. Sergeev, N. Vagidov, and K. Reinhardt, Strong enhancement of solar cell efficiency due to quantum dots with built-in charge, Nano Lett. **11,** 2311 (2011).

[25] A. Zrenner, E. Beham, S. Stufler, F. Findeis, M. Bichler, and G. Abstreiter, Coherent properties of a two-level system based on a quantum-dot photodiode, Nature (London) **418,** 612 (2002).

[26] A. J. Ramsay, S. J. Boyle, R. S. Kolodka, J. B. B. Oliveira, J. Skiba-Szymanska, H. Y. Liu, M. Hopkinson, A. M. Fox, and M. S. Skolnick, Fast Optical Preparation, Control, and Readout of a Single Quantum Dot Spin, Phys. Rev. Lett. **100,** 197401 (2008).

[27] J. D. Mar, J. J. Baumberg, X. Xu, A. C. Irvine, and D. A. Williams, Ultrafast high-fidelity initialization of a quantum-dot spin qubit without magnetic fields, Phys. Rev. B **90,** 241303 (2014).

[28] T. Nozawa, H. Takagi, K. Watanabe, and Y. Arakawa, Direct observation of two-step photon absorption in an InAs/GaAs single quantum dot for the operation of intermediate-band solar cells, Nano Lett. **15,** 4483 (2015).

[29] M. Bayer, G. Ortner, O. Stern, A. Kuther, A. A. Gorbunov, A. Forchel, P. Hawrylak, S. Fafard, K. Hinzer,

T. L. Reinecke, S. N. Walck, J. P. Reithmaier, F. Klopf, and F. Schäfer, Fine structure of neutral and charged excitons in self-assembled In(Ga)As/(Al)GaAs quantum dots, Phys. Rev. B **65,** 195315 (2002).

[30] J. D. Mar, X. L. Xu, J. J. Baumberg, F. S. F. Brossard, A. C. Irvine, C. Stanley, and D. A. Williams, Bias-controlled single-electron charging of a self-assembled quantum dot in a two-dimensional-electron-gas-based *n-i*-Schottky diode, Phys. Rev. B **83,** 075306 (2011).

[31] K. Peng, S. Wu, J. Tang, F. Song, C. Qian, S. Sun, S. Xiao, M. Wang, H. Ali, D. A. Williams, and X. Xu, Probing the Dark-Exciton States of a Single Quantum Dot Using Photocurrent Spectroscopy in a Magnetic Field, Phys. Rev. Applied **8,** 064018 (2017).

[32] J. D. Mar, J. J. Baumberg, X. L. Xu, A. C. Irvine, C. R. Stanley, and D. A. Williams, High-resolution photocurrent spectroscopy of the positive trion state in a single quantum dot, Phys. Rev. B **87,** 155315 (2013).

[33] J. D. Mar, X. L. Xu, J. J. Baumberg, A. C. Irvine, C. Stanley, and D. A. Williams, Voltage-controlled electron tunneling from a single self-assembled quantum dot embedded in a two-dimensional-electron-gas-based photovoltaic cell, J. Appl. Phys. **110,** 053110 (2011).

[34] J. D. Mar, X. L. Xu, J. J. Baumberg, A. C. Irvine, C. Stanley, and D. A. Williams, Electrically tunable hole tunnelling from a single self-assembled quantum dot embedded in an n-i-Schottky photovoltaic cell, Appl. Phys. Lett. **99,** 031102 (2011).

[35] H. S. Nguyen, G. Sallen, C. Voisin, P. Roussignol, C. Diederichs, and G. Cassabois, Optically Gated Resonant Emission of Single Quantum Dots, Phys. Rev. Lett. **108,** 057401 (2012).

[36] A. J. Bennett, J. P. Lee, D. J. P. Ellis, T. Meany, E. Murray, F. F. Floether, J. P. Griffths, I. Farrer, D. A. Ritchie, and A. J. Shields, Cavity-enhanced coherent light scattering from a quantum dot, Sci. Adv. **2,** e1501256 (2016).

[37] G. Moody, C. McDonald, A. Feldman, T. Harvey, R. P. Mirin, and K. L. Silverman, Electronic Enhancement of the Exciton Coherence Time in Charged Quantum Dots, Phys. Rev. Lett. **116,** 037402 (2016).

[38] A. Kurzmann, A. Ludwig, A. D. Wieck, A. Lorke, and M. Geller, Auger recombination in self-assembled quantum dots: Quenching and broadening of the charged exciton transition, Nano Lett. **16,** 3367 (2016).

[39] E. Beham, A. Zrenner, F. Findeis, M. Bichler, and G. Abstreiter, Nonlinear ground-state absorption observed in a single quantum dot, Appl. Phys. Lett. **79,** 2808 (2001).

[40] W. Heller, U. Bockelmann, and G. Abstreiter, Electric-field effects on excitons in quantum dots, Phys. Rev. B **57,** 6270 (1998).

[41] R. Oulton, J. J. Finley, A. D. Ashmore, I. S. Gregory, D. J. Mowbray, M. S. Skolnick, M. J. Steer, S.-L. Liew, M. A. Migliorato, and A. J. Cullis, Manipulation of the homogeneous linewidth of an individual In(Ga)As quantum dot, Phys. Rev. B **66,** 045313 (2002).

[42] S. Cao, J. Tang, Y. Gao, Y. Sun, K. Qiu, Y. Zhao, M. He, J.-A. Shi, L. Gu, D. A. Williams, W. Sheng, K. Jin, and X. Xu, Longitudinal wave function control in single quantum dots with an applied magnetic field, Sci. Rep. **5,** 8041 (2015).